



Engineering the Protective Oxide Chemistry for Enhanced Corrosion Protection Performance of FeCuCrNiCo-CNT Composite Coatings in 3.5 M NaCl Solution Corrosive Media

SUJATA SINGH and CHANDAN SRIVASTAVA

Direct electrodeposition method was used to co-electrodeposit different volume fractions of carbon nanotubes in FeCuCrNiCo high entropy alloy matrix. Phase constitution, morphology, wettability, protective oxide film chemistry, and corrosion behavior of the composite coatings were studied as a function of volume fraction of carbon nanotubes (CNTs). Pristine HEA coating contained mixture of body-centered cubic (bcc) and face-centered cubic (fcc) phases which transformed into nearly single-phase body-centered cubic microstructure with the incorporation of CNTs upto a certain optimum volume fraction. The phase heterogeneity, however, re-appeared for higher CNT additions. The coating morphology showed a transition from one containing mixture of dendritic and granular features to a more compact, smooth, and fine-grained globular matrix with CNT incorporation. A monotonic increase in the water contact angle was also observed with increasing CNT content in the composite coating. Weight loss and potentiodynamic polarization techniques employed for coating corrosion analysis showed that the corrosion behavior of pristine coating was highly sensitive to the amount of reinforced CNTs. Addition of an optimum CNT amount in HEA coating (produced from an electrolyte with 12.5 mg/L of dispersed CNTs) led to a considerable decrease (85.6 pct) in the corrosion rate (compared to the pristine HEA coating). In addition to improved morphology, phase homogenization, and increased contact angle, the reason for this significant improvement was also attributed to the evolution of protective oxides like Cr_2O_3 and NiO in case of HEA-CNT composite with optimum CNT concentration. For higher CNT additions, a drastic decrease in the protection efficiency was observed because of re-appearance of phase heterogeneity. This promoted galvanic coupling and due to the presence of surface defects in forms of cracks arising due to the presence of agglomerated CNTs in the electrodeposited coatings.

<https://doi.org/10.1007/s11661-023-06994-1>

© The Minerals, Metals & Materials Society and ASM International 2023

I. INTRODUCTION

HIGH entropy alloys (HEA) are alloys with multiple principle elements in equimolar or nearly equimolar ratios.^[1,2] When all the constituent elements in an alloy are equi-atomic, then the configurational entropy of the system reaches its maximum. When five elements are alloyed, the value of configuration entropy (1.61 R) exceeds the melting entropy of the metallic elements with usual values of 1.1 to 1.3 R, thus preventing the

formation of intermetallics and favoring the simple solid solutions to form. Due to the vast scope of design possible and their varied structural as well as functional properties, HEAs possess excellent attributes like good thermal stability, extremely high hardness, fracture toughness, electrical and magnetic properties, and excellent corrosion resistance.^[2-4] Due to their remarkable properties, various methods such as arc melting, mechanical alloying, additive manufacturing, rapid solidification,^[3] *etc.* have been developed to fabricate HEAs. For synthesizing HEA thin films/coatings, methods like magnetron sputtering, laser cladding, chemical-vapor deposition, plasma transfer arc cladding, electro-spark deposition, electrochemical deposition,^[5,6] *etc.* are typically employed.

Among the many HEA systems, FeCuCrNiCo system, which satisfies the Hume-Rothery criterion, is a well-explored HEA system.^[7] Studies are available in the

SUJATA SINGH and CHANDAN SRIVASTAVA are with the Department of Materials Engineering, Indian Institute of Science, Bangalore 560012, India. Contact e-mail: csrivastava@iisc.ac.in
Manuscript submitted October 23, 2022; accepted January 25, 2023.

Article published online February 20, 2023

literature on the corrosion behavior of this HEA system. Hsu *et al.*^[8] studied about the influence of addition of varying amount of copper ($x = 0, 0.5, \text{ and } 1$) on the corrosion resistance of the as-cast FeCoNiCrCu_{*x*} alloys and reported the reason for deterioration in corrosion resistance with increased Cu addition was the galvanic coupling between cathodic Cu-depleted, Cr-rich region and anodic Cu-rich, and Cr-depleted dendritic regions. In a similar system, Garip *et al.*^[9] used mechanical milling and reported that Fe₂CoCrNi_{0.5}Si_{0.25}Cu_{0.25} showed the best and Fe₂CoCrNi_{0.5}Cu_{0.25} HEAs showed the worst corrosion resistance. This observation highlighted the positive impact of silicon which forms dense and well-adherent scale acting as protective barrier to permeation of corrosive electrolyte. In addition to this, in case of Fe₂CoCrNi_{0.5}Si_{0.25}Cu_{0.25}, the detrimental effects of copper's poor adherence of scale with the substrate led to decreased corrosion resistance. In another study, Qiu *et al.*^[10] reported that as compared to Q235 carbon steel substrate, the current density of laser clad Al₂CoCrCuFeNiTi_{*x*} and Al₂CoCrCuFeTiNi_{*x*} HEA coatings reduced by two orders of magnitude when exposed to 0.5 M HNO₃ and 0.6 M NaCl solutions. The reason for such improved corrosion behavior was strong metallurgical bonding with the substrate and formation of equiaxed grains. Moreover, the rapid cooling and high entropy helped in reducing the segregation gradient, thus, homogenizing microstructure.

Another approach to engineer the corrosion properties of HEAs is to reinforce the HEA matrix with minor amounts of foreign additives like Cerium, SiC, Al₂O₃, WC, TiC, TiN, TiB₂, NbC^[11–14] as well as with carbonaceous additives^[15,16] like graphene, carbon nanotubes, and graphene oxide. Though researchers have reported on HEAs as promising corrosion resistance material, one of the challenges limiting the application of HEA for corrosion inhibition is phase inhomogeneity stemming primarily from the elemental segregation within the HEA matrix. Such microstructural inhomogeneity promotes undesirable galvanic coupling and accelerated corrosion. This study addresses the issue of phase heterogeneity in FeCuCrNiCo HEA coatings (as a candidate system) through the incorporation of CNTs in the HEA matrix using a cost-effective, scalable, and less equipment intensive electrodeposition method.^[17] The need for such study arises from the fact that corrosion destroys more than 3 pct of world's Gross Domestic Product. One way of development of functional materials which can survive in extremely corrosive environments is to induce hydrophobicity to the otherwise hydrophilic metallic surfaces. With this idea, we reinforced hydrophilic metallic High Entropy Alloys with hydrophobic and chemically inert hydrophobic CNTs. The present study provides an insight into the corrosion behavior of FeCuCrNiCo HEA as a function of volume fraction of CNT and discusses the underlying reasons for the same, which to the best of our knowledge is not yet reported in literature.

II. EXPERIMENTAL SECTION

The CNTs used in this study were synthesized using the chemical vapor deposition method. Details on the synthesis, functionalization, and characterization of CNTs are provided in the authors previous work.^[16]

Pristine FeCuCrNiCo and FeCuCrNiCo-CNT composite coatings were electrodeposited using a chloride-based acidic electrolyte over mild steel substrate. The optimized deposition parameters and bath compositions are given in Table I. Mechanically polished mild steel plate was used as cathode, and platinum foil and Ag/AgCl were used as the counter electrode and reference electrode, respectively. Direct current was used for electrodeposition, and NaOH was used to adjust the pH of the bath. Apart from the metal salts, various additives such as gelatin, cetyltri-ammonium bromide, ammonium chloride, boric acid, ascorbic acid, sulphanyllic acid, and formic acid were added to the electrolyte to improve the bonding between elements, enable co-deposition of elements with varying reduction potentials, and to attain uniform surface morphology. After the synthesis, the electrodeposited surface was rinsed with distilled water and dried. Since, the reduction potentials of all the elements involved in electrodeposition vary widely (Cr = - 0.74 V, Fe = - 0.44 V, Co = - 0.28 V, Ni = - 0.25 V, Cu = + 0.34 V), therefore to co-deposit multi-component HEAs coatings, the metal salts were taken in inverse proportion with respect to their reduction potential values.

To identify the crystal structure and phases of synthesized coatings, X'pert Pro Panalytical X-ray Diffractometer was used to obtain diffraction patterns. The machine equipped with CuK α ($\lambda = 0.1542 \text{ nm}$) radiation source was operated at 40 kV and 30 mA with 0.033 deg as 2 Θ step size. Optical micrographs of the coatings were obtained using a Leica DMi8 model optical microscope equipped with a charge coupled device. FEI ESEM Quanta 200 SEM coupled with an energy-dispersive X-ray spectroscopy detector was employed for the surface morphological characterization and for obtaining the elemental composition of the HEA/HEA-CNT composite coatings. Surface roughness measurements were conducted using Veeco Dektak surface profilometer. A 2 μm stylus radius was used at low-scan speed of 10 $\mu\text{m/s}$ over a scan length of 1000 μm . Measurement resolution was 0.33 $\mu\text{pt.}$ and scan time was 10 s. The profilometer was maintained a constant stylus force of 3 mg as the sample stage moved the sample under the stylus tip to trace a profile. To further understand how the CNTs in the electrolyte interacted with metallic ions, Zeta potential measurements were conducted using Zetasizer Nanoseries-ZEN 3690 (Malvern Instruments). Six sets of electrolytes were prepared by dissolving individual metal salts in separate solution containing dispersed CNTs. The concentration of individual metal salts (in individual solutions) was same as taken in the electrolytic bath for electrodeposition (Table I). An electrolyte containing only dispersed CNT was taken as the control. Hydrophobicity test was

Table I. Bath Chemistry and Optimized Parameters

Sample	Bath Composition	Concentration (g/L)	Condition
HEA	FeCl ₂ ·4H ₂ O NiCl ₂ ·6H ₂ O CoCl ₂ ·6H ₂ O CrCl ₃ ·4H ₂ O CuCl ₂ ·2H ₂ O	0.50 2.75 0.95 2.40 0.10	current density: 45 mA/cm ² temperature: 28 ± 1 °C time of deposition 15 min pH 1.5 (with stirring)
HEA_C1	FeCoNiCrCu with CNT	1.56 mg/L	
HEA_C2		3.13 mg/L	
HEA_C3		6.25 mg/L	
HEA_C4		12.50 mg/L	
HEA_C5		25.00 mg/L	
HEA_C6		50.00 mg/L	

conducted by sessile drop test method using OCA 15EC optical contact angle measuring system equipped with goniometer, a microsyringe, a light source, and a camera with a macro lens. A 1 μ L deionized water droplet was dropped on the coatings and soaked for 30 seconds to attain equilibrium. The tangent of the sessile drop profile at the contact point with the surface was used to find contact angles. An instrument CHI 604E was employed to perform corrosion tests. The corrosive media used for corrosion tests were 3.5 M NaCl solution, which is equivalent to sea-water environment. Firstly, the open circuit potential was recorded for one hour and stabilized. With respect to the obtained OCP values, the working electrode was polarized to ± 200 mV and scanned at 1 mV/s to obtain potentiodynamic polarization curves. The frequency range used for electrochemical impedance studies was 100 kHz to 0.001 Hz with the sinusoidal signal amplitude of 5 mV. The data obtained were interpreted using the ZSimpWin 3.21 software and by fitting with the equivalent electrical circuit model. Composition of the passive film of the exposed coatings was determined using the ESCA+ (omicron nanotechnology, Oxford Instrument Germany) X-ray photoelectron spectroscopy. The monochromator aluminum source (Al K _{α} radiation at 1486.7 eV) equipped instrument was operated at 15 kV and 15 mA with 20 eV and 50 eV pass energy for short and survey scans, respectively. The CasaXPS software was used to analyze XPS data and the peaks were fitted by the mixed Gaussian–Lorentzian functions after Shirley background subtraction. The binding energy scale was calibrated at 284.5 eV for a C1s peak, and all the other peaks were calibrated by the standard C1s peak.

III. RESULTS AND DISCUSSION

A. Phase Constitution-XRD

Diffraction patterns of electrodeposited pristine HEA and HEA-CNT composite coatings are shown in Figure 1(a). None of the diffraction patterns showed peaks corresponding to individual component elements, thus confirming the formation of solid solution. The

pristine HEA coating contained a mixture of major face-centered cubic phase with minor fraction of body-centered cubic phase, consistent with the published reports.^[15,18]

With increase in the CNT content, a continuous decrease in volume fraction of the fcc (111) peak together with an increase in the volume fraction of bcc (110) peak was observed, indicating the evolution of nearly single-phase BCC solid solution for HEA_C4 coating. Beyond this (higher additions of CNTs), the amount of the FCC phase again increased leading to a mixed phase microstructure (as indicated by the changes in the relative peak intensities in the XRD pattern). This observation indicated that CNT incorporation into the FeCuCrNiCo matrix modifies the coatings phase constitution significantly.

The crystallite size for FCC and BCC phases was calculated using Scherrer formula.^[15] The relative decrease in crystallite size for both phases till HEA_C4 followed by an increase is presented in Figure 1(b). Initially, as a result of uniform dispersion of CNT, heterogeneous sites for nucleation sites increased, resulting in reduced average crystallite size.^[16] The trend however reversed for higher CNT additions due to the agglomeration of CNTs owing to their high surface energy. The observed fine crystallite size was due to sluggish diffusion involved in high entropy alloy systems.^[1–4]

The phase homogenisation is shown more clearly in Figure 2, by the deconvolution of the FCC and BCC phase peaks in the XRD pattern between 40 and 47 deg. Fraction (calculated using the peak intensities) of the BCC phase increased from 56.26 pct in HEA coating to 91.8 pct in HEA_C4 coating coupled with reduction in the volume fraction of FCC phase from 43.74 pct for HEA coating to 8.03 pct. This shows that CNTs enhance phase and compositional homogeneity. The trend, however, reversed beyond the optimum CNT volume fraction (HEA_C4) as phase separation was again noticed at higher incorporation of CNTs. This could be due to the agglomeration of the CNTs in the electrolyte bath which retards the homogenous dispersion and decreases the amount of metal–CNT interfaces in the coating matrix. The percentages of both phases are given in Table II.

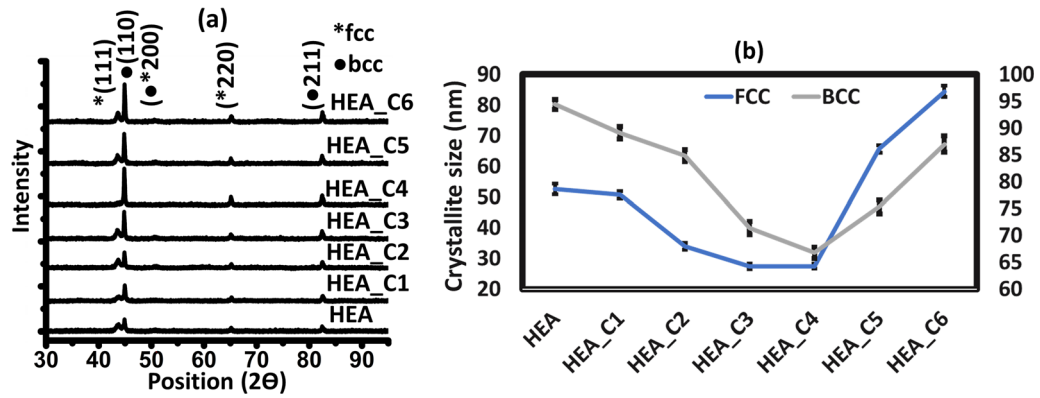


Fig. 1—(a) XRD patterns of HEA and HEA-CNT composite coatings, (b) Crystallite size of fcc and bcc phases.

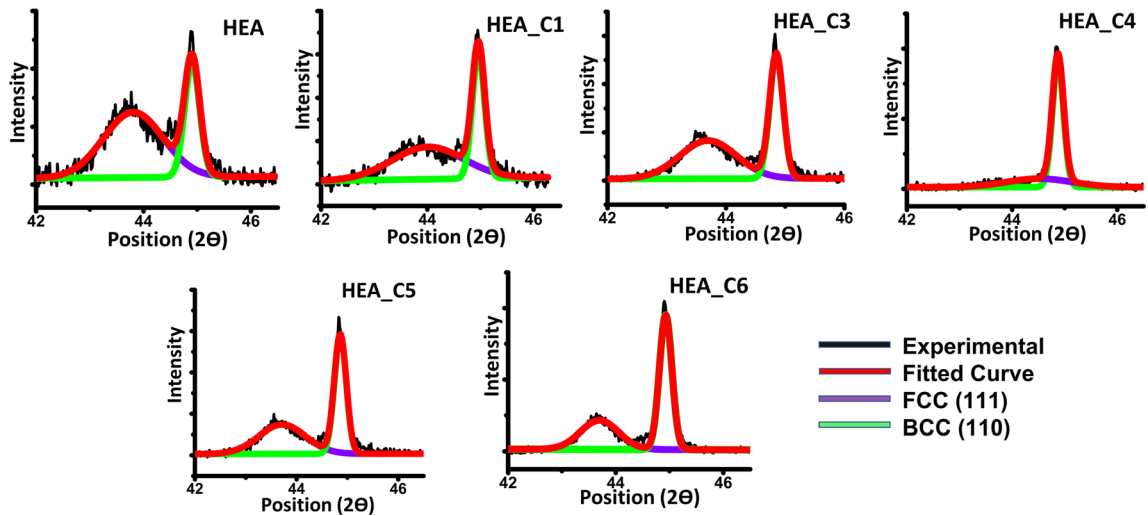


Fig. 2—Deconvoluted XRD peaks in the 2θ range of 40 to 47 deg.

B. Morphological and Compositional Effects

1. Optical images

Figure 3 shows the optical micrograph of the as-deposited HEA coatings with and without CNTs. The optimized bath chemistry and operating parameters led to the synthesis of continuous coatings with good surface coverage and crack-free morphology. With the addition of CNTs, the coating smoothness progressively increased till HEA_C4 and the coatings appeared relatively rough for the last two additions (HEA_C5 and HEA_C6).

2. Morphology-SEM

Addition of CNTs was observed to significantly affect the morphology of the HEA coatings as shown in Figure 4. Two distinct morphologies were clearly visible in the pristine FeCuCrNiCo coating: the dendritic features which segregated itself from the matrix and the globular matrix. The dendritic features were copper-rich (shown below) owing to the high enthalpy of mixing of Cu with other elements.^[15,16,18,19] The enthalpy of mixing is given in Table III. CNT addition promoted phase homogenization by dissolving the

dendritic phase into the matrix. Moreover, with CNT addition the morphology transformed from dendritic to granular, which is known to lower the corrosion rate.^[5] The coating progressively became more fine-grained because CNT addition provided more heterogeneous sites for nucleation of grains. Additionally, the tubular structure of CNTs, known to fill up non-uniformities on the coating surface, rendered coating surface relatively compact and smooth, which made the surface more corrosion-resistant.^[20] All these beneficial effects could be attributed to uniform dispersion of CNTs in the coatings till HEA_C4. Beyond this threshold concentration, cracked morphology was observed, which aggravated on further addition of CNTs (HEA_C5 and HEA_C6 coatings). This was because the uniform dispersion of CNTs in the electrolyte bath becomes difficult beyond a threshold concentration and they tend to agglomerate thus degrading the coating compactness.

C. Coating Composition

An increase in carbon content from HEA_C1 to HEA_C6 (Table IV) was noted which indicated increase in CNT content of coating. It should be noted that these

Table II. Variation in BCC and FCC Phase Fraction with Increase in CNT Concentration

Sample/Phase Concentration (Atomic Percent)	BCC Percent	FCC Percent
HEA	56.26	43.74
HEA_C1	59.57	40.42
HEA_C2	62.42	37.58
HEA_C3	66.40	30.93
HEA_C4	91.80	8.03
HEA_C5	61.17	38.82
HEA_C6	60.55	60.55

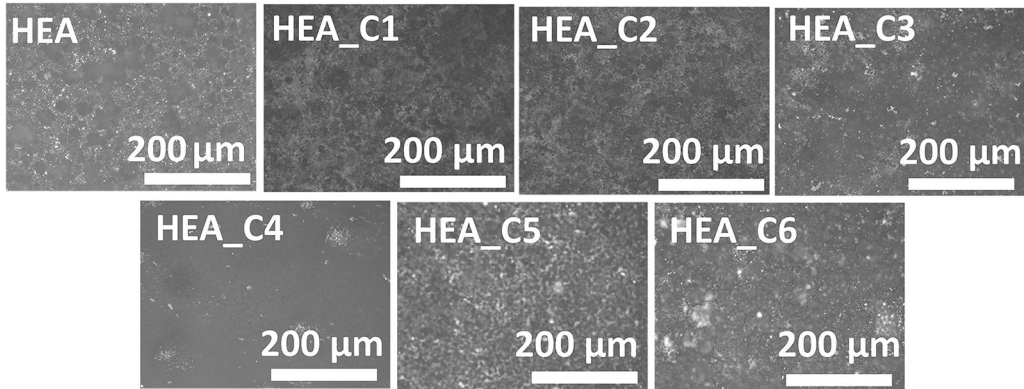


Fig. 3—Optical images of the as-deposited HEA and HEA-CNT composite coatings.

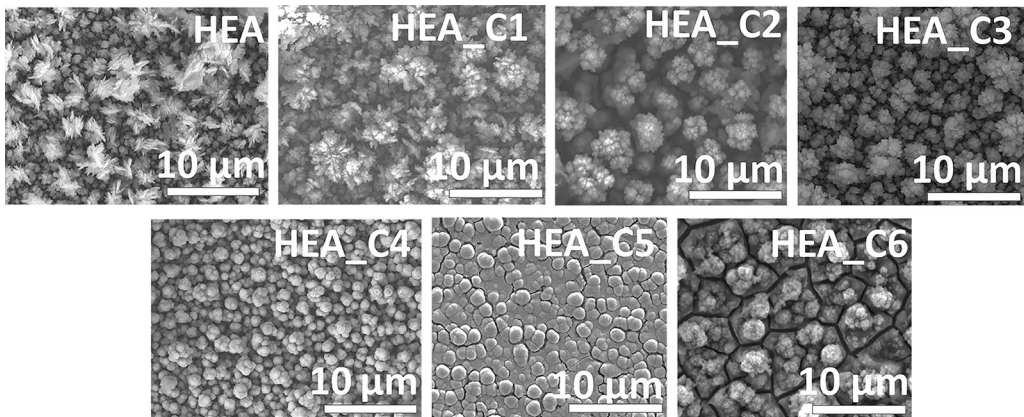


Fig. 4—SEM micrographs showing morphological changes with CNT addition.

Table III. Enthalpy of Mixing Values for Different Element Pairs

Elements	$\Delta H^{\text{mix}}_{AB}$				
	Cr	Ni	Co	Fe	Cu
Cr	—				
Ni	− 7	—			
Co	− 4	0	—		
Fe	− 1	− 2	− 1	—	
Cu	12	4	6	13	—

absolute values have contributions from other carbonaceous additives (kept constant in all the electrolytic bath) as well. Therefore, only the increasing trend should be considered. Moreover, the average composition of the coatings showed a steady rise in chromium concentration and depletion in copper concentration reaching nearly uniform composition till HEA_C4 as shown in Figure 5.

This compositional trend agrees with the observations from the diffraction patterns. Increase in chromium content is responsible for increase in the BCC phase, and decrease in copper leads to depletion in the FCC phase fraction with CNT addition. Beyond HEA_C4,

Table IV. Quantitative Carbon Content in Electrodeposited Coatings Obtained by SEM-EDS Analysis

Element/System	HEA	HEA_C1	HEA_C2	HEA_C3	HEA_C4	HEA_C5	HEA_C6
	0.6 ± 0.02	1.02 ± 0.22	2.43 ± 0.43	3.86 ± 0.86	5.7 ± 0.51	7.8 ± 1.82	12.4 ± 2.04

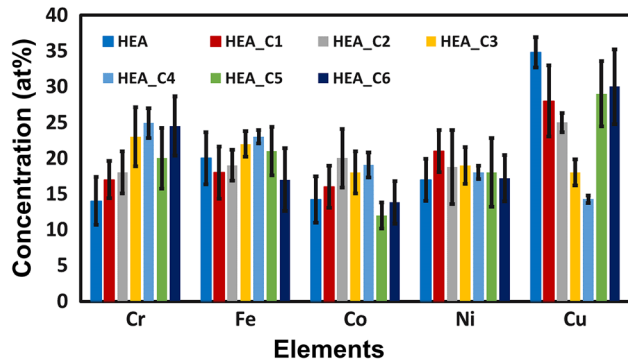


Fig. 5—Histograms showing average elemental composition of HEA and HEA-CNT composites.

the FCC Cu-rich phase re-appeared leading to phase and compositional heterogeneity in the coating matrix. The compositional partitioning is observed in Figure 6 where spot 1 and spot 2 represent two different regions in the coating. It was observed that the dendritic phase predominantly contained copper (~ 66 at. pct) with minor amounts of other elements. The matrix phase contained all elements with composition slightly higher in iron and chromium content.

HEA_C4 exhibited highest compositional homogeneity. For highest CNT addition, spot compositional analysis showed a heterogeneity in a way that copper content increased in phase corresponding to spot 1 and chromium increased in phase corresponding to spot 2. Several cracks could also be seen in HEA_C6 coating owing to the presence of agglomerated CNTs in the matrix.

The focused ion beam scanning electron microscope (FEI Helios SEM-FIB instrument) was used to look into the interfacial bonding between mild steel substrate and coating as well as to measure the thickness of HEA and HEA_C4 coating. To prevent the damage caused by the Gallium ions, platinum was deposited over the region of interest. The observed thickness for HEA and HEA_C4 was in the range of 5 ± 0.15 and $5.2 \pm 0.26 \mu\text{m}$, respectively. The observed slight increase in thickness of coating in case of HEA_C4 could be attributed to the swelling tendency that CNTs impart because of their tubular structure. Moreover, the images show excellent adherence of coating with the substrate (Figure 7).

D. CNT Distribution and Surface Roughness

The way CNTs are distributed in the matrix affects the coating morphology and ultimately its electrochemical behavior. Figure 8 shows the homogeneous distribution of CNTs in the matrix in case of HEA_C4. The

cracked morphology in HEA_C6 could be attributed to the agglomerated CNTs near the grain boundaries.^[21]

Surface roughness and irregularities on the surface form nucleation sites for cracks or defects aiding corrosion initiation. As shown in Figure 9, profilometry tests qualitatively revealed that the addition of optimum CNT volume fraction helped in lowering the roughness. The reason for such observation can be clearly understood from Figure 8 which shows uniformly distributed CNTs in HEA_C4 and agglomerated CNTs in HEA_C6 coating.

E. Zeta Potential

The degree of electrostatic repulsion between charged particles in a dispersion can be measured by Zeta Potential values.^[22] It is basically the potential difference that is required to keep two charged particles separated. Conversely, the lower the Zeta potential, the greater the affinity of charged particles for adsorption. Based on this idea, separate experiment was designed to find out which out of the five component elements does CNT adsorbs preferentially. Six different baths comprising of (a) well-dispersed CNTs (used as standard), (b) Fe-CNT, (c) Cu-CNT, (d) Cr-CNT, (e) Ni-CNT, and (f) Co-CNT bath were prepared for Zeta potential measurements. It was observed that the Zeta potential value followed the trend: Cr-CNT < Ni-CNT < Fe-CNT < Co-CNT < Cu-CNT which indicated toward the preference of CNTs for chromium adsorption over other elements (Figure 10). This revealed the reason for increase in the BCC phase fraction and Cr content with CNT addition.

F. Contact Angle Measurement

Water contact angle substantially affects the corrosion rate in aqueous-based corrosive media.^[23] Figure 11 shows the variation of contact angle, with images of deionized water droplet profile, on the coating surface. The contact angles of water droplets over HEA coating, HEA_C4 coating, and HEA_C6 coating were found to be 80.8 ± 0.21 , 136.0 ± 0.25 , and 138.5 ± 0.23 deg, respectively. It was observed that the contact angle value increased substantially with the incorporation of the CNTs, but changed very marginally beyond HEA_C4 coating. Using Cassie-Baxter equation mentioned below, we can calculate the fraction of coating surface area in contact with water, which in turn, affects wettability:

$$\cos \theta_r = f_1 \cos \theta - f_2, \quad [1]$$

where θ = contact angle of HEA coating, θ_r = contact angle of HEA-CNT coating, f_1 = fraction of solid,

f_2 = fraction of air at the solid–liquid interface. A decrease in the fraction of solid–liquid interface area means reduced space that water occupies on the coating. Thus, an increase in the contact angle increases the fraction of air pockets at the interface. The fraction of air pockets at the interface of HEA_C4 coating was calculated to be 75.79 pct. The presence of such large fraction of superhydrophobic air at the interface enhanced the anti-corrosion behavior by preventing the permeation of the corrosive electrolyte from entering the coating surface.^[24]

IV. CORROSION ANALYSIS

A. Weight Loss Analysis Method

Weight loss method, a destructive mode of exploring corrosion rate, was used to estimate the formation and degradation of passive film over the coating surface. The method involved weighing of the as-synthesized coatings followed by immersing them in 3.5 wt pct NaCl solution for 1, 12, 24, 36, and 48 hours and finally subtracting the

final weight of the exposed coatings from the initial weight of the electrodeposited coatings. Before the final weight measurement, the exposed coatings were washed thoroughly and dried in ambient atmosphere. The following equation was used to evaluate corrosion rate in millimeters per year (mm/y)^[25]:

$$\text{Corrosion rate (CR)} = \frac{K \times W}{A \times T \times \rho_{\text{alloy}}}, \quad [2]$$

where K is a constant with value of 8.76×10^4 , W is weight loss in grams, A is the electrodeposited area (4 cm^2) of the coating, T is the exposure time in hours (h), and ρ_{alloy} is the density of the alloy (g/cm^3). The density of alloys and incurred weight loss were calculated using the relation below:

$$\text{Density of alloys } \rho_{\text{alloy}} = \sum_{j=1}^n (\rho_j \times f_j) \quad [3]$$

$$\text{Weight loss (W)} = W_{\text{initial}} - W_{\text{aftertime (t)}} \quad [4]$$

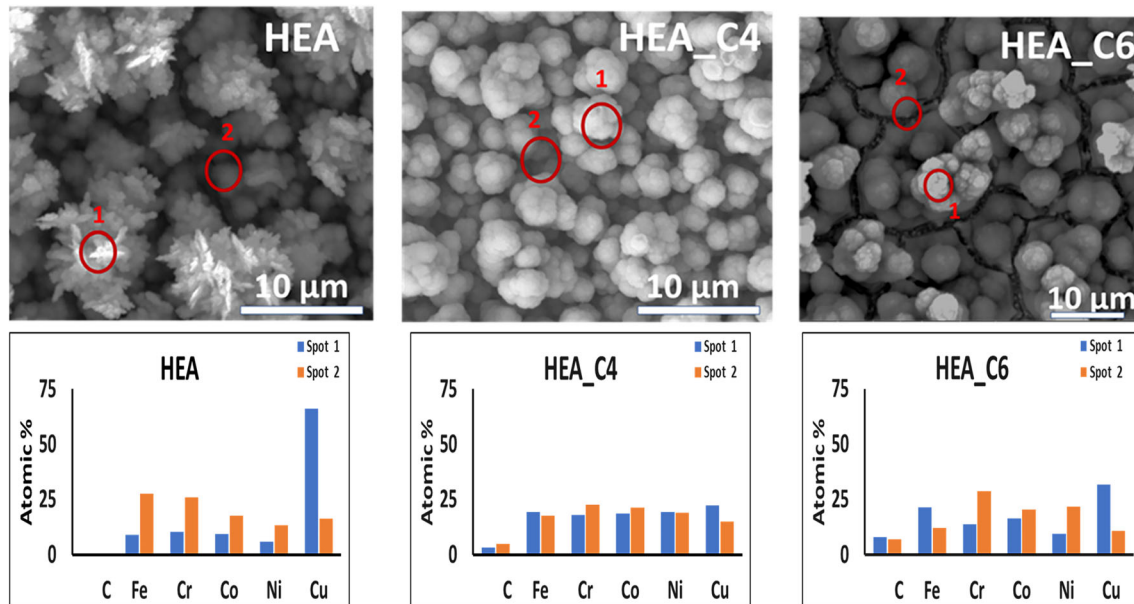


Fig. 6—Histogram showing compositional homogenization by spot EDS analysis.

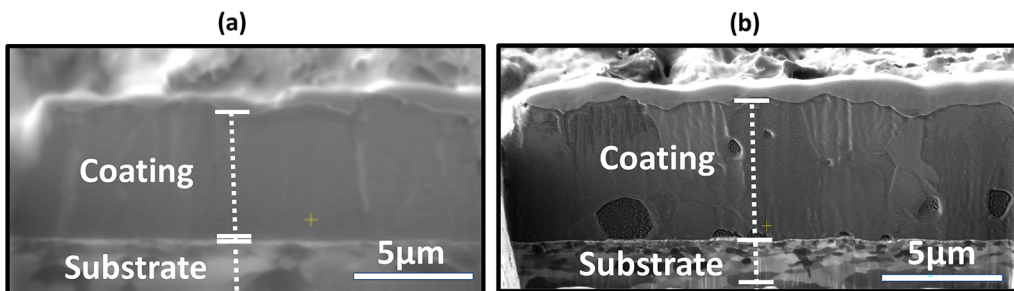


Fig. 7—SEM-FIB cross-sectional SEM lamellar micrograph of (a) pristine HEA, and (b) HEA_C4 coating.

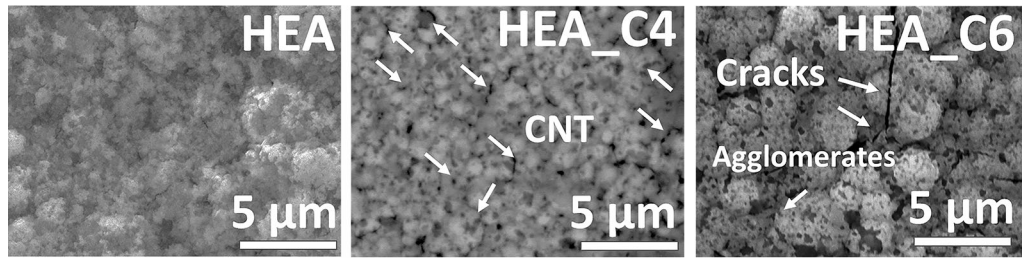


Fig. 8—Micrographs showing HEA and CNT distribution in HEA_C4 and HEA_C6 coatings.

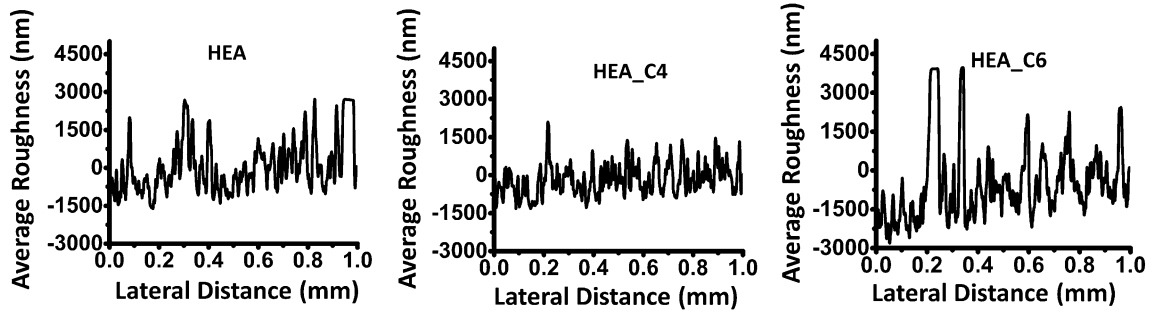


Fig. 9—Surface roughness profile as obtained by Dektak Profilometer.

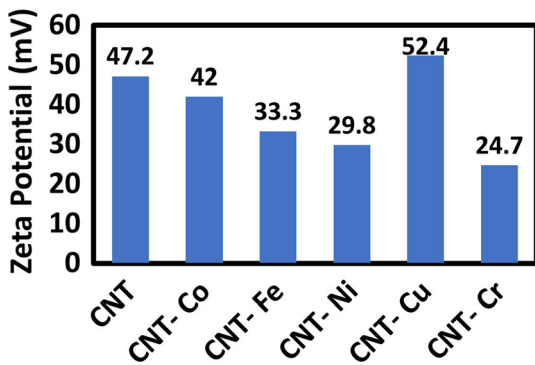


Fig. 10—Zeta potential variation of CNT and metal-CNT electrolytes.

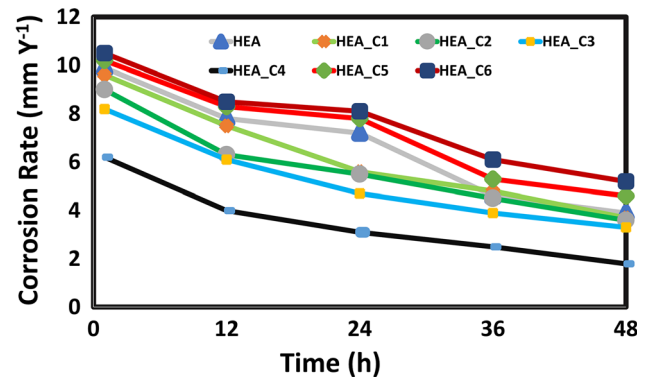


Fig. 12—Corrosion rate of HEA and HEA-CNT composite coatings as a function of immersion time in 3.5 wt pct NaCl solution.

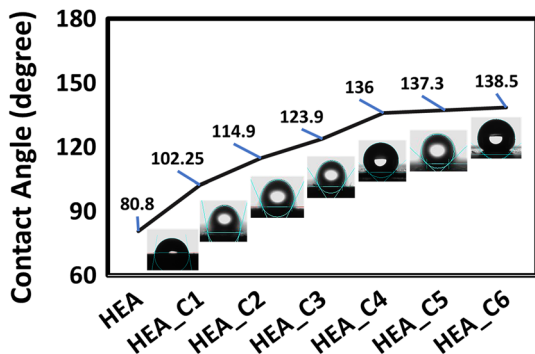


Fig. 11—Variation of water contact angle with CNT addition.

The results clearly showed that the HEA_C4 coating exhibited the lowest weight loss when compared to the weight loss of all other coatings for all the exposure times. It is apparent from the plot (Figure 12) that for the initial 1 hour exposure, the corrosion rate reduced by 39 pct for HEA_C4 coating as compared to pristine HEA coating. Similar rate of decline in weight loss was noticed for all the coatings till 12 hours of exposure. In the case of HEA, the slope between 12 and 24 hours was gradual, indicating formation of relatively stable oxide film followed by a steep slope beyond 24 hours indicated degradation of the oxide film formed. Whereas, in case of HEA_C4, from 1 to 48 hours, remarkably gradual

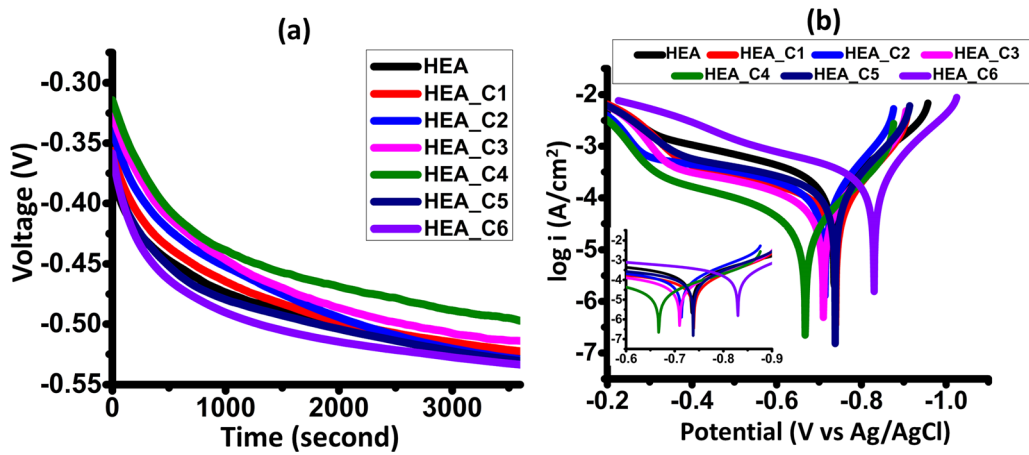


Fig. 13—(a) Open circuit potential, (b) Tafel polarization plots of FeCuCrNiCo and FeCuCrNiCo-CNT coatings.

Table V. Electrochemical Parameters Derived from Tafel Polarization Plot

Sample/Parameter	E_{corr} (V)	I_{corr} ($\mu\text{A}/\text{cm}^2$)	Corrosion Rate ($\text{mil}/\text{y}/\text{cm}^2$)	Linear Polarization (Ω/cm^2)	β_c (dec/V)	β_a (dec/V)
HEA	-0.736	169.3	35.32	232	7.12	3.97
HEA_C1	-0.714	94.56	19.72	346	9.69	3.61
HEA_C2	-0.739	69.51	14.50	482	9.45	3.54
HEA_C3	-0.710	54.33	11.33	631	8.68	4.01
HEA_C4	-0.667	24.27	5.06	1416	8.07	4.59
HEA_C5	-0.738	113.4	23.65	310	8.91	3.47
HEA_C6	-0.830	216.6	45.17	165	8.50	3.64

decline in the slope was noticed, which indicated the formation of stabler protective oxide film on the composite coating surface.

B. Potentiodynamic Polarization Test

1. Open circuit potential and tafel polarization behavior

The open circuit potential (E_{ocp}) values were first stabilized for 1 hour to achieve a constant value. It is well known, the potential shift toward a more positive value is an indication of better anti-corrosion behavior.^[5] It was observed that the CNT incorporation till 12.5 mg/L CNT concentration led to a positive shift in potential values indicating lower susceptibility toward corrosion (Figure 13(a)). This trend was reversed for the next two coatings which showed a negative shift in the E_{ocp} values.

Figure 13(b) displays the polarization curves of electrodeposited coatings in 3.5 M NaCl solution (which replicates sea-water corrosion) under their respective and stable OCP conditions. The anodic branch of the polarization curve showed passivation behavior, which is indicative of the presence of oxides and hydroxides on the surface. For further evaluation, the linear region of anodic and cathodic polarization curves was extrapolated to derive the relevant parameters like corrosion potential, corrosion current density, Tafel slopes,

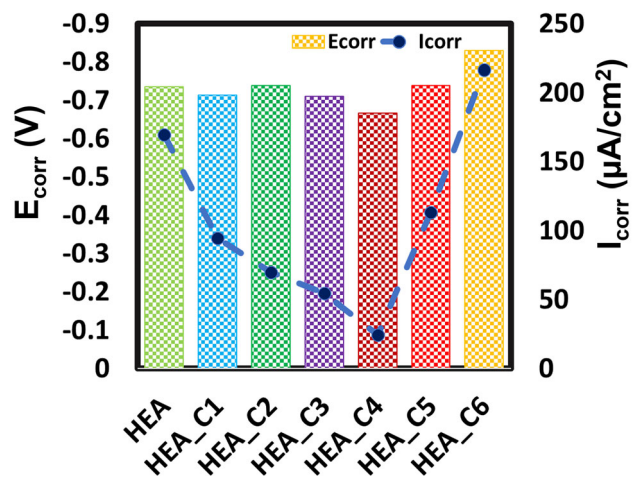


Fig. 14—Plot showing variation of E_{corr} and I_{corr} of HEA and HEA-CNT composite coatings.

corrosion rate, and linear polarization resistance, and the values of which are tabulated in Table V.

It can be observed that the E_{corr} values showed a positive shift from -0.736 V for pristine HEA coatings to -0.667 V for HEA_C4 coating followed by a negative shift till -0.830 V for HEA_C6 coating, implying the highest corrosion susceptibility. Also, in terms of corrosion current density, a decrease in the I_{corr}

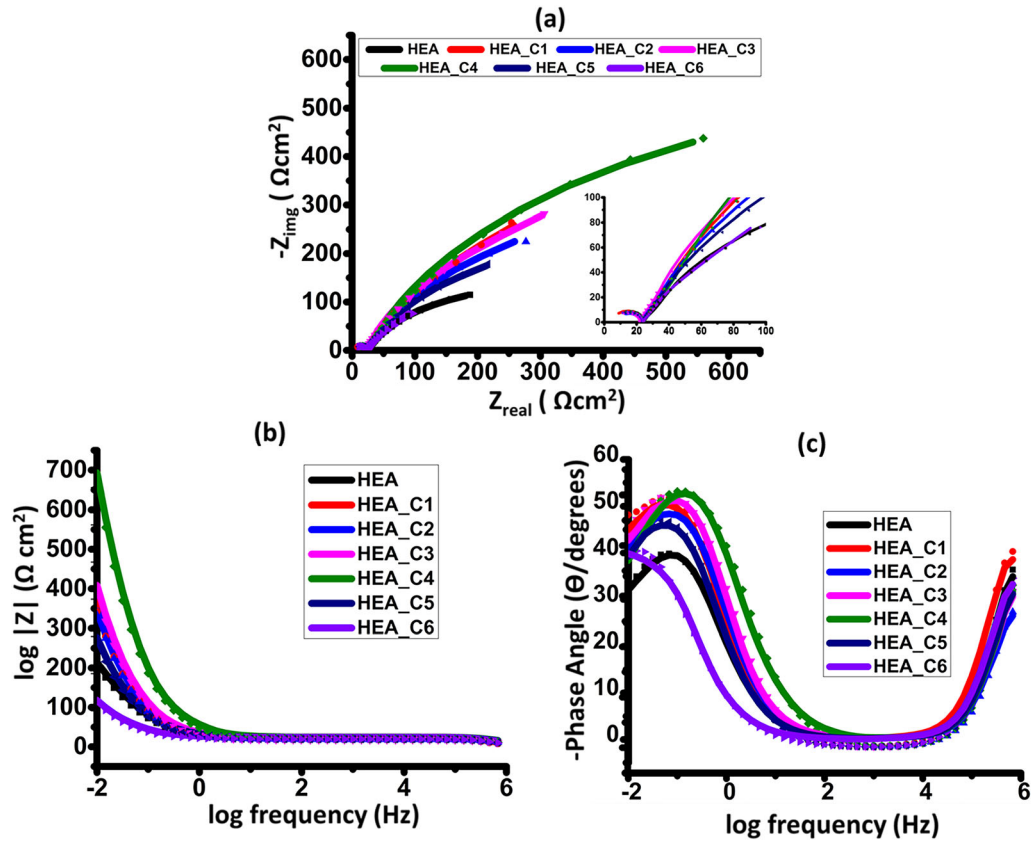


Fig. 15—(a) Nyquist impedance plots, (b) Bode's impedance plot, and (c) Bode's phase angle plot.

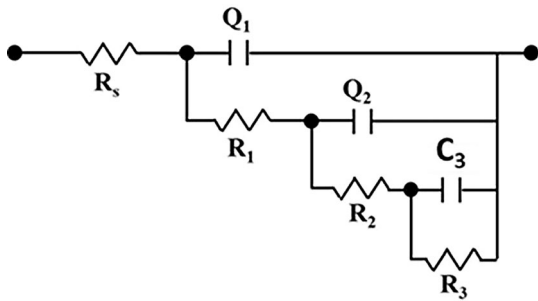


Fig. 16—Electrochemical equivalent circuit used to simulate EIS data.

value from $169.3 \mu\text{A}/\text{cm}^2$ for pristine HEA to $24.27 \mu\text{A}/\text{cm}^2$ for the HEA_C4 coating followed by a further step rise till $216.6 \mu\text{A}/\text{cm}^2$ was observed. Moreover, a remarkable decrease in the corrosion rate from $35.32 \text{ mil}/\text{year}/\text{cm}^2$ for pristine HEA to $5.06 \text{ mil}/\text{year}/\text{cm}^2$ for HEA_C4 coating together with a sharp increase thereafter, reaching $216.6 \text{ mil}/\text{year}/\text{cm}^2$ for the highest CNT addition (HEA_C6) was noted. It is well known that electropositive E_{corr} and low corrosion current density (I_{corr}) indicate higher corrosion resistance of the material.^[5,26] Thus, the results suggest that HEA_C4 has the best corrosion resistance performance among all the coatings.

Therefore, the trend shown in Figure 14 is indicative of improved corrosion resistance of the coating with

incorporation of an optimum volume fraction of CNTs in the pristine HEA coating. The protection efficiency of HEA_C4 was found to be 85.66 pct as compared to the HEA coating.

2. Electrochemical impedance spectroscopy

Electron Impedance Spectroscopy method was employed to understand the characteristics of the surface film and the corrosion process mechanism.^[26,27] The solid lines and symbols represent the measured data and simulated data, respectively. Nyquist plots (Figure 15(a)) comprised of flattened capacitive semicircle of different diameters in the low-frequency region, while the loops diameters at high frequencies were almost similar. As compared to the pristine HEA, the radius of the impedance curve revealed an increasing trend till HEA_C4 and started to decrease thereafter demonstrating an increment in the corrosion resistance capacity due to reinforcement of an optimum amount of CNT (till HEA_C4) followed by deterioration in anti-corrosive property with higher CNT concentration. The larger the radius of the semicircle, the lower the frequency and longer the period, which means slower electrochemical reaction kinetics and better corrosion resistance performance.^[27,28] The curve in Figure 15(b) showed that in high-frequency region, the $|Z|$ values are close together, whereas they move apart in low-frequency region. High corrosion resistance is characterized by an upward shift in $|Z|$ value together with higher

Table VI. Fitting Parameters Values Obtained from EEC Simulation of EIS Data

Sample/ Parameter	R_s (Ω / cm^2)	Q_1 10^{-8} ($\Omega^{-1}/$ cm^2/S^n)	n_1	R_1 (Ω cm^2)	Q_2 ($\Omega^{-1}/$ cm^2/S^n)	n_2	R_2 (Ω cm^2)	F ($\Omega^{-1}/$ cm^2/S^n)	R_3 (Ωcm^2)	R_p (Ω cm^2)	Chi square E^{-4}
HEA	6.00	2.70	0.98	18.55	0.017	0.59	170.2	0.1005	473.8	662.5	3.30
HEA_C1	5.36	2.84	0.99	18.39	0.015	0.74	720.7	0.0052	743.1	1482.2	4.76
HEA_C2	8.32	2.27	1.00	14.06	0.015	0.71	809.8	0.003	1134.0	1957.9	7.74
HEA_C3	6.30	2.92	0.97	15.7	0.010	0.63	963.2	0.003	1352.0	2330.9	4.98
HEA_C4	6.79	2.18	0.98	17.7	0.006	0.67	1290.0	0.0007	1633.0	2940.7	5.35
HEA_C5	6.91	2.56	0.98	16.8	0.016	0.62	372.8	0.004	812.1	1201.8	3.30
HEA_C6	6.73	2.31	0.99	16.9	0.051	0.67	200.9	0.014	305.3	523.18	3.30

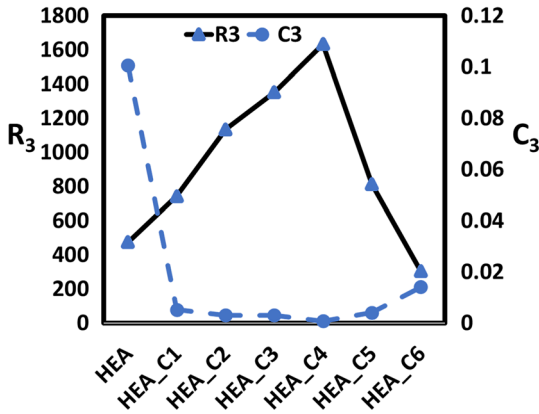


Fig. 17—Variation of R_3 and C_3 as obtained from EIS simulation.

and broadened phase angle as shown in Figure 15(c), both of which could be observed in HEA_C4 coating. All these observations indicated the corrosion rate to be highly sensitive to the amount of CNT and with increase in the CNT amount upto a particular concentration, a relatively robust barrier formed which reduced the active surface area thus abated further corrosion process.

Simulation of the coated area and corrosive solution interface was done by fitting the Nyquist curves with the hypothetical electrical equivalent circuit model using Zsimp win 3.21 software (Figure 16). The oxygen reduction associated with formation of corrosion products is characterized by low-frequency regime, whereas the charge transfer resistance and pore resistance are defined by medium and high-frequency region.

To account for the non-uniformity in potential and distribution of current as a result of defects on the coating surface, the ideal capacitance was replaced by a constant phase element ‘ Q ’,^[26,28] the impedance of which is defined as

$$Z_{\text{CPE}} = \frac{1}{Q(j\omega)^n}, \quad [5]$$

where Q is CPE constant, j is an imaginary unit, $\omega = 2\pi f$, and n is empirical constant ranging from 0 to 1.

In the EEC model, R_1 represents the resistance due to ionic leakage through pores and Q_1 represents the

capacitance corresponding to the high-frequency region. R_2 and Q_2 , the mid-frequency components appear as a result of oxidation–reduction reactions occurring in the passive layer formed. R_3 depicts the charge transfer resistance and Q_3 represents the double layer capacitance. The solution resistance, R_s , acting between working and reference electrode was found to be nearly same for all coatings. Polarization resistance (R_p), calculated as sum of all the resistances in high-, mid-, and low-frequency region, is an important parameter indicating corrosion resistance capabilities of coatings^[27] and is highest for HEA_C4 (2940.7 Ωcm^2).

Various parameters obtained from the EEC model are tabulated in Table VI. An excellent fit between the model and the experimental data (χ^2 values in the range of 10^{-4}) was noted. The decrease in value of Q_2 indicated reduced surface activity which in turn increased R_2 . With further corrosion, more corrosion products formed, thickening the barrier layer between the surface of coating and the corrosive media. This further led to reduction of C_3 (till HEA_C4), and as a result, R_3 increased. As a result, an increase in R_2 and R_3 value coupled with decrease in Q_2 and Q_3 value (till HEA_C4) was observed. From Figure 17, the opposite trend observed in variation of C_3 and R_3 against the addition of CNTs clearly emphasized the importance of reinforcing the coating with an optimum concentration of CNT to achieve highest corrosion resistance. It is to be noted that the EIS analysis goes hand-in-hand with the potentiodynamic polarization analysis.

V. XPS

A. Survey Spectrum

Since, the anodic curves in Tafel polarization showed passivation behavior and the EIS analysis indicated formation of surface oxides after exposure to the corrosive media, further investigation of the passive surface oxide chemistry was conducted using XPS technique. Figure 18 displays the survey spectra of pristine HEA coating and the one with highest corrosion resistance *i.e.*, HEA_C4. The survey spectra showed that all the elements (Fe, Cu, Cr, Ni, Co, O) were detectable on the surface of both samples.

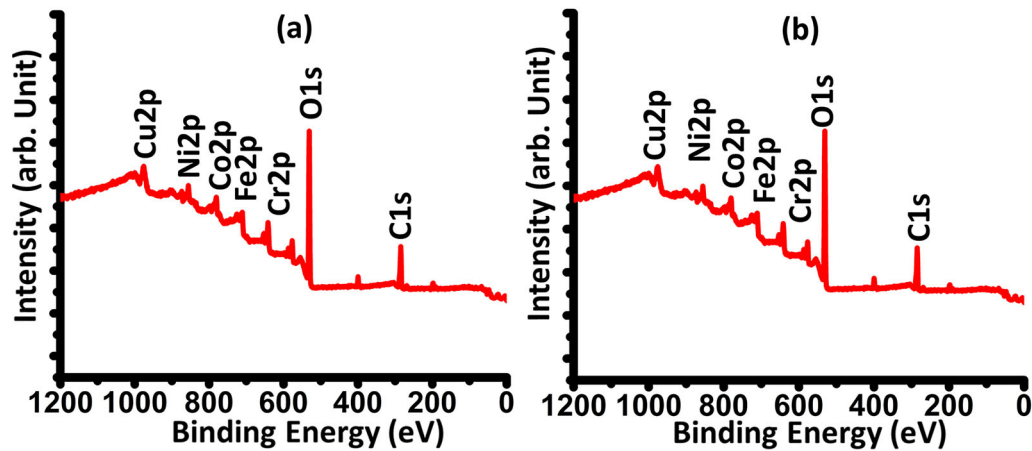


Fig. 18—Survey spectrum of (a) HEA, and (b) HEA_C4 coatings showing the presence of individual elements after corrosion in sea-water media.

B. High-Resolution XPS Spectra

To know more about the oxidation states in which elements are present on the surface of the coatings, high-resolution spectra from the signals corresponding to Fe $2p_{3/2}$, Cr $2p_{3/2}$, Cu $2p_{3/2}$, Ni $2p_{3/2}$, and Co $2p_{3/2}$ were used. Careful deconvolution and peak fitting were carried out for each photoelectron peak, and the corresponding fitting curves are shown in Figure 19. The open symbols represent the experimental data and the solid lines through the open symbols represent the overall fitting curves. The spectra of Fe $2p_{3/2}$ were divided into three components: Fe⁰, Fe²⁺ (Fe₂O₃), and Fe³⁺ (Fe₃O₄) oxide, Cu $2p_{3/2}$ spectra were deconvoluted into Cu⁰ and Cu²⁺ (CuO). The Co $2p_{3/2}$ spectra were deconvoluted into constituent peaks, namely, metallic Co⁰, Co²⁺ (CoO), and Co³⁺ (Co₃O₄). The spectrum of Cr $2p_{3/2}$ was divided into three components, *i.e.*, Cr⁰, Cr³⁺ (Cr₂O₃), and Cr⁶⁺ (Cr(OH)₃). Fe $2p_{3/2}$ spectra were split into the peaks corresponding to the metallic Fe⁰, Fe_{ox}²⁺ (FeO), Fe_{ox}³⁺ (Fe₂O₃), and Fe_{hy}³⁺ (Fe(OH)₃). The metallic Ni⁰, Ni_{ox}²⁺ (NiO), and Ni_{hy}²⁺ (Ni(OH)₂) were the deconvoluted peaks corresponding to Ni $2p_{3/2}$ spectra. The O 1s spectrum was decomposed into two peaks for HEA (O²⁻ and OH⁻) and an additional bound H₂O peak for HEA_C4. Table VII tabulates the binding energies of the corresponding peaks which is consistent with the literature reports.^[29–31]

C. Quantitative Analysis-Cationic Fraction

Table VIII shows the relative contents of various states in which Fe, Cu, Cr, Ni, and Co elements are present in the passive oxide film. The calculated percentage abundance of each constituent is directly proportional to the intensity or area under the photoelectron peaks. After immersion in the corrosive media, as expected, the concentration of oxides or hydroxides was more than the elemental state. In HEA, the Fe_{ox}³⁺ and Fe_{hy}³⁺ were the dominant constituent of iron, whereas in HEA_C4, it was Fe_{ox}²⁺. Literature says that Fe²⁺ (FeO) is more protective than Fe³⁺ (Fe₂O₃

and FeOOH) which was substantiated by a study which reported that increased Fe₂O₃ of passive film on 304 austenitic stainless steel deteriorated the corrosion resistance in deionized water, whereas higher FeO content made the passive layer more stable, thus enhancing corrosion resistance. Moreover, Fe₂O₃, more commonly known as rust, being powdery and flaky, cannot operate as protective barrier against subsequent corrosion. The Fe²⁺/Fe³⁺ ratios expressed as FeO/(Fe₂O₃ + FeOOH) ratios were much higher in case of HEA_C4 coating. Reports suggest that the density of FeO being higher than Fe₂O₃, the former formed more robust and compact protective layer and led to enhancement of the corrosion resistance.^[32] Among the two stable states in which Co is present, Co³⁺ is well known for stabilizing the passive film^[33] and as revealed from Figure 19, Co³⁺ is more dominantly present over Co²⁺ in case of HEA_C4 coating.

Unlike other elements, the predominant form of Nickel present in the passive film of HEA is metallic Nickel. The reason being the lower oxidation kinetics which arises as a result of electronic configuration being characterized by fully filled *d* orbitals.^[34] The existence of Ni²⁺ oxide in HEA_C4 may be due to its slower diffusion rate compared to other elements and was found to be one of the dominant oxides on HEA_C4 surface.

Since, the pristine HEA contained FCC phase in form of copper-rich phase, after corrosion, CuO, the oxidized form of copper, was the most predominant oxide on the HEA surface. Based on literature, it was found that copper and its oxides are detrimental for corrosion properties because Cu degrades the compactness of the films by reducing the passivation ability and thus enhances the charge transfer in HEA films leading to easy breakdown of film in chloride environment thus resulting in deterioration of anti-corrosion behavior.^[35,36]

The un-equivocal benefit of Cr₂O₃ toward the corrosion resistance has been recognized by several authors in different systems.^[32–37] It is apparent that surface oxide

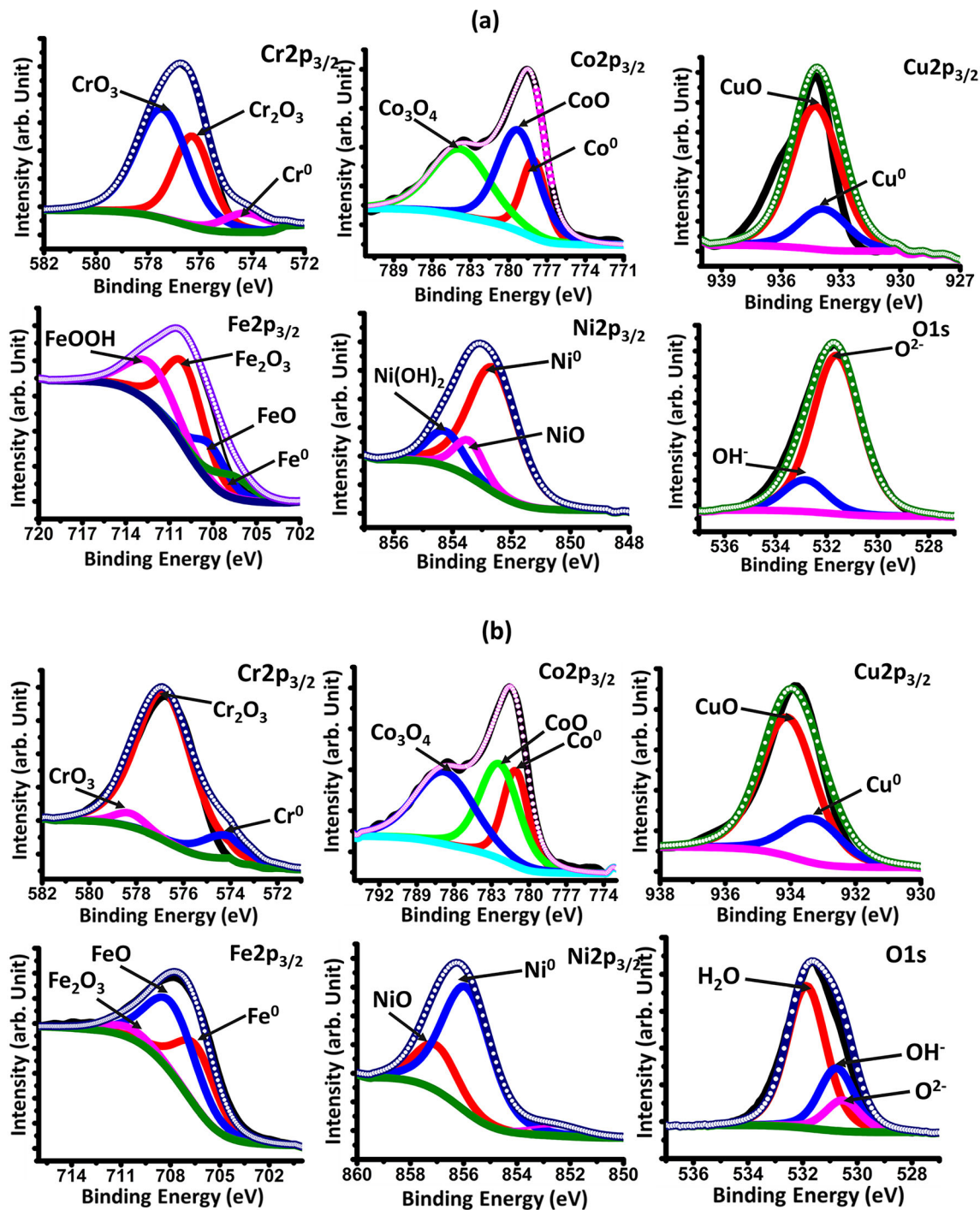


Fig. 19—High-resolution XPS spectra of passive film of (a) HEA, and (b) HEA_C4 coating after corrosion where open circles: experimental data and solid lines: overall fitting curves.

film of HEA_C4 was enriched with Cr_2O_3 . The ratio of Cr_2O_3 and metallic Cr was calculated to be almost three times in the case of HEA_C4 when compared to HEA. In HEA, Cr is present in Cr^{6+} form which has defective, porous, and unstable structure. Additionally, peak corresponding to bound water (H_2O), present in HEA_C4, forms an additional protection barrier layer by capturing the dissolved metal ions.^[32] However, for

HEA, the peak corresponding to H_2O in the passive film was absent. The quantitative volume fractions of metallic and cationic species of all the elements in the passive film of HEA and HEA_C4 are shown in Figure 20.

Based on the cationic fraction plot data, the concentration of metallic elements and their oxides the sequence of decreasing order is mentioned below:

Table VII. Binding Energies of Deconvoluted XPS Spectra of Individual Elements

Element	Oxidation State	HEA Peak Position	HEA-C4 Peak Position
Fe	Fe ⁰	706.7	706.7
	FeO	708.2	707.9
	Fe ₂ O ₃	709.9	710.7
	FeOOH	712.5	—
Cr	Cr ⁰	574.2	574.2
	Cr ₂ O ₃	576.3	576.8
	CrO ₃	577.5	578.4
Cu	Cu ₀	933.8	933.9
	CuO	934.6	934.6
Ni	Ni ⁰	852.6	852.6
	NiO	853.3	855.3
	Ni(OH) ₂	853.5	856.4
Co	Co ⁰	778.1	778.2
	CoO	779.4	779.9
	Co ₃ O ₄	783.8	783.6
O	O ²⁻	531.1	530.5
	OH ⁻	532.1	531.9
	H ₂ O	—	532.0

Table VIII. Relative Contents of Fe, Cr, Cu, Ni, Co in Various States on Passive Film Formed on Surface of HEA and HEA_C4

Element	Oxidation State	HEA Percent Concentration	HEA_C4 Percent Concentration
Fe	Fe ⁰	1.31	9.27
	FeO	1.85	16.75
	Fe ₂ O ₃	4.72	2.39
	FeOOH	2.86	0.00
Cr	Cr ⁰	6.74	3.06
	Cr ₂ O ₃	6.96	20.23
	CrO ₃	11.68	1.19
Cu	Cu ₀	4.98	1.09
	CuO	17.51	3.04
Ni	Ni ⁰	8.88	6.76
	NiO	4.35	11.77
	Ni(OH) ₂	3.24	2.73
Co	Co	8.90	1.74
	CoO	12.46	4.26
	Co ₃ O ₄	2.80	9.28

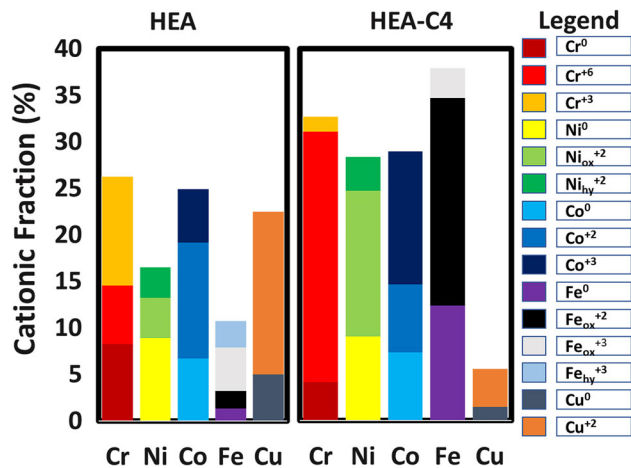


Fig. 20—Cationic fractions in passive film of HEA and HEA_C4 coatings.

For HEA: CuO > CoO > Co₃O₄ > CrO₃ > Ni⁰ > Cr₂O₃ > Co⁰ > Cu⁰ > Fe₂O₃ > NiO > Ni(OH)₂ > FeOOH > FeO > Cr⁰ > Fe⁰

For HEA_C4: Cr₂O₃ > Fe⁰ > FeO > Co₃O₄ > NiO > Ni⁰ > CoO > Co⁰ > CuO > Ni(OH)₂ > Fe₂O₃ > CrO₃ > Cu⁰

According to the abovementioned sequence, Cr₂O₃ is the main component in the passive film formed in HEA_C4, while in case of the HEA, it is CuO. This confirms that the film formed on HEA_C4 is more stable, which can provide better protection.

VI. CONCLUSIONS

The effect of incorporation of CNTs on the phase constitution, surface morphology, composition, hydrophobicity, and electrochemical behavior of FeCuCrNiCo high entropy alloy coating was investigated. The key findings of the study are as follows:

1. Diffraction pattern of pristine HEA coating showed a phase mixture of FCC and BCC. Upon the incorporation of CNTs, the FCC phase fraction diminished, while the BCC phase fraction grew reaching almost a single-phase BCC microstructure. Beyond an optimum CNT concentration, phase inhomogeneity re-appeared.
2. Upon the incorporation of CNTs, the coatings became fine-grained, smooth, and more compact because of the uniform dispersion of CNTs. At higher CNT concentrations, cracks developed and coating surface became rougher. Addition of CNTs favored increase in Cr content in the coating. This was the reason for the increasing BCC phase fraction with CNT incorporation.
3. Contact angle measurement showed that CNT imparted hydrophobicity (with contact angle of 136 deg for HEA_C4 coating) to the otherwise hydrophilic pristine coatings (with a contact angle of 80.80 deg for HEA coating). Beyond the threshold CNT, the contact angle increased insignificantly.
4. Cationic fraction plots (derived from XPS analysis) showed that major constituents of the protective passive oxide film in HEA are Cr^{6+} , $\text{Ni}_{\text{hy}}^{2+}$, Co^{3+} , $\text{Fe}_{\text{hy}}^{3+}$ as compared to HEA_C4, which had more stable species Cr^{3+} , $\text{Ni}_{\text{ox}}^{2+}$, Co^{2+} , Fe^{2+} as primary constituents. The coating with highest corrosion resistance was predominantly enriched with Cr_2O_3 which is known for its highly protective nature against corrosive media. Moreover, the presence of bound water formed additional protection layer by capturing the dissolved metal ions.
- 53 All the results showed that with an optimum volume fraction of CNT, the corrosion resistance significantly enhanced with the protection efficiency reaching 85.66 pct for HEA_C4 coating. Beyond this threshold, the surface defects caused by agglomerated CNTs undermined the benefits offered by CNTs against corrosion protection.

ACKNOWLEDGMENTS

The authors acknowledge the research funding received from the SERB Government of India.

CONFLICT OF INTEREST

On behalf of all authors, the corresponding author states that there is no conflict of interest.

REFERENCES

1. B. Cantor, I.T.H. Chang, P. Knight, and A.J.B. Vincent: *Mater. Sci. Eng. A*, 2004, vol. 375–377, pp. 213–18.
2. D.B. Miracle and O.N. Senkov: *Acta Mater.*, 2017, vol. 122, pp. 448–511.
3. K.M. Youssef, A.J. Zaddach, C. Niu, D.L. Irvin, and C.C. Koch: *Mater. Res. Lett.*, 2015, vol. 3, pp. 95–99.
4. A.A. Rempel and B.R. Gelchinski: *Steel Transl.*, 2020, vol. 50, pp. 243–47.
5. Y. Shi, B. Yang, and P.K. Liaw: *Metals*, 2017, vol. 7, pp. 1–8.
6. X.L. Shang, Z.J. Wang, H.E. Feng, J.C. Wang, J.J. Li, and J.K. Yu: *Sci. China Technol. Sci.*, 2018, vol. 61, pp. 189–96.
7. Y.F. Ye, Q. Wang, J. Lu, C.T. Liu, and Y. Yang: *Mater. Today Commun.*, 2016, vol. 19, pp. 349–62.
8. Y.J. Hsu, W.C. Chiang, and J.K. Wu: *Mater. Chem. Phys.*, 2005, vol. 92, pp. 112–17.
9. Y. Garip: *Corros. Sci.*, 2022, vol. 206, p. 110497.
10. X.-W. Qiu and C.-G. Liu: *J. Alloys Compd.*, 2013, vol. 553, pp. 216–20.
11. Y. Guo, X. Shang, and Q. Liu: *Surf. Coat. Technol.*, 2018, vol. 344, pp. 353–58.
12. X. Li, Y. Feng, B. Liu, D. Yi, X. Yang, W. Zhang, G. Chen, Y. Liu, and P. Bai: *J. Alloys Compd.*, 2019, vol. 788, pp. 485–94.
13. J. Cheng, D. Liu, X. Liang, and Y. Chen: *Surf. Coat. Technol.*, 2015, vol. 281, pp. 109–16.
14. J.-W. Yeh: *Eur J Control*, 2006, vol. 31, pp. 633–48.
15. A. Aliyu, M.Y. Rekha, and C. Srivastava: *Philos. Mag.* 2018, vol. 99, pp. 1–18.
16. S. Singh, S.M. Shaikh, M.K.P. Kumar, B.S. Murty, and C. Srivastava: *Materialia*, 2020, vol. 14, p. 100917.
17. M.J. Popescu, F. Branzoi, I. Constantin, M. Anastasescu, M. Burada, D. Mitric, I. Anasiei, M.-T. Olaru, and V. Constantin: *Coatings*, 2021, vol. 11, p. 1367.
18. S. Praveen, B.S. Murty, and R.S. Kottada: *Mater. Sci. Eng. A*, 2012, vol. 534, pp. 83–89.
19. S. Ozturk, F. Alptekin, S. Onal, S.E. Sunbul, O. Sahin, and K. Icin: *J. Alloys Compd.*, 2022, vol. 903, p. 163867.
20. A. Singh, T. Ram Prabhu, A.R. Sanjay, and V. Koti: *Mater. Today: Proc.*, 2017, vol. 4, pp. 3872–881.
21. R.I. Rubel, M.H. Ali, M.A. Jafor, and M.M. Alam: *AIMS Mater. Sci.*, 2019, vol. 6, pp. 756–80.
22. D. Wang, Y. Xu, D. Xiao, Q. Qiao, P. Yin, Z. Yang, J. Li, W. Winchester, Z. Wang, and T. Hayat: *J. Hazard. Mater.*, 2019, vol. 371, pp. 83–93.
23. R. Ramachandran and M. Nosonovsky: *Phys. Chem*, 2015, vol. 17, pp. 24988–4997.
24. T. Zheng, Y. Hu, Y. Zhang, and F. Pan: *J. Colloid Interface Sci.*, 2017, vol. 505, pp. 87–95.
25. K. Baratpour: *ASTM*, 2004, vol. G31–72, pp. 1–8.
26. R. Mishra and R. Balasubramaniam: *Corros. Sci.*, 2004, vol. 46, pp. 3019–029.
27. S. Wang, J. Zhang, O. Gharbi, V. Vivier, M. Gao, and M.E. Orazem: *Nat. Rev. Methods Prim.*, 2021, vol. 41, pp. 1–21.
28. C. Ji, A. Ma, and J. Jiang: *J. Alloys Compd.*, 2022, vol. 900, p. 163508.
29. M. Liu, X. Cheng, X. Li, Y. Pan, and J. Li: *Appl. Surf. Sci.*, 2016, vol. 389, pp. 1182–191.
30. S. He and D. Jiang: *Int. J. Electrochem. Sci.*, 2018, vol. 13, pp. 5822–849.

31. W.A. Badawy, F.M. Al-Kharafi, and J.R. Al-Ajmi: *J. Appl. Electrochem.*, 2000, vol. 30, pp. 693–704.
32. J.-Y. Jiang, D. Wang, H.-Y. Chu, H. Ma, Y. Liu, Y. Gao, J. Shi, and W. Sun: *Materials (Basel)*, 2017, vol. 10, pp. 1–2.
33. H. Luo, Z. Li, A.M. Mingers, and D. Raabe: *Corros. Sci.*, 2018, vol. 134, pp. 131–39.
34. M. Steimecke, G. Seiffarth, C. Schneemann, F. Oehler, S. Förster, and M. Bron: *ACS Catal.*, 2020, vol. 10, pp. 3595–603.
35. T. Xi, M.B. Shahzad, D. Xu, Z. Sun, J. Zhao, C. Yang, M. Qi, and K. Yang: *Mater. Sci. Eng. C*, 2017, vol. 17, pp. 1079–085.
36. M. Seo, G. Hultquist, C. Leygraf, and N. Sato: *Corros. Sci.*, 1986, vol. 26, pp. 949–60.
37. L. Huang, X. Wang, X. Zhao, C.Z. Wang, and Y. Yang: *Mater. Chem. Phys.*, 2021, vol. 259, p. 124007.

Publisher's Note Springer Nature remains neutral with regard to jurisdictional claims in published maps and institutional affiliations.

Springer Nature or its licensor (e.g. a society or other partner) holds exclusive rights to this article under a publishing agreement with the author(s) or other rightsholder(s); author self-archiving of the accepted manuscript version of this article is solely governed by the terms of such publishing agreement and applicable law.